Hindawi
Mathematical Problems in Engineering
Volume 2020, Article ID 3108589, 18 pages
https://doi.org/10.1155/2020/3108589

Research Article

Research on Curved Path Tracking Control for Four-Wheel Steering Vehicle considering Road Adhesion Coefficient

Runqiao Liu,[1] **Minxiang Wei**,[1] **Nan Sang**,[2] **and Jianwei Wei**[3]

[1]*Department of Vehicle Engineering, Nanjing University of Aeronautics & Astronautics, Nanjing 210016, Jiangsu, China*
[2]*Department of Vehicle Engineering, Changzhou Institute of Technology, Changzhou 213002, Jiangsu, China*
[3]*Department of Automotive Engineering, Ningbo University of Technology, Ningbo 315336, Zhejiang, China*

Correspondence should be addressed to Minxiang Wei; vbe@nuaa.edu.cn

Received 14 October 2019; Revised 14 December 2019; Accepted 26 December 2019; Published 20 January 2020

Academic Editor: Ramon Sancibrian

Curved path tracking control is one of the most important functions of autonomous vehicles. First, small turning radius circular bends considering bend quadrant and travel direction restrictions are planned by polar coordinate equations. Second, an estimator of a vehicle state parameter and road adhesion coefficient based on an extended Kalman filter is designed. To improve the convenience and accuracy of the estimator, the combined slip theory, trigonometric function group fitting, and cubic spline interpolation are used to estimate the longitudinal and lateral forces of the tire model (215/55 R17). Third, to minimize the lateral displacement and yaw angle tracking errors of a four-wheel steering (4WS) vehicle, the front-wheel steering angle of the 4WS vehicle is corrected by a model predictive control (MPC) feed-back controller. Finally, CarSim® simulation results show that the 4WS autonomous vehicle based on the MPC feed-back controller can not only significantly improve the curved path tracking performance but also effectively reduce the probability of drifting or rushing out of the runway at high speeds and on low-adhesion roads.

1. Introduction

Path tracking control enables autonomous vehicles to travel accurately, smoothly, and safely along a predetermined path and to remain stable under all driving conditions [1]. As early as 1980, MacAdam [2] proposed an optimal preview path tracking control method, which could minimize the tracking error in channel-changing simulation. Currently, this control method has been applied to the path tracking model in CarSim® software [3]. In addition, the model predictive control (MPC) method can easily handle the nonholonomic constraints of a vehicle system and solve the trade-off problem between path tracking and driving safety [4]. Due to these advantages, many researchers have studied the MPC path tracking method. Borrelli et al. [5] presented a nonlinear MPC approach for active front-wheel steering control. Katriniok and Abel [6] used a predictive controller based on a linear time-varying model (LTV-MPC) to minimize tracking error and response lag. Kim et al. [7] used an MPC path tracking control method based on quadratic programming (QP) optimization to improve the path tracking performance of autonomous vehicles. Schwarting et al. [8] used a receding horizon planner based on nonlinear model predictive control (NMPC) to ensure safety collision avoidance. However, the above control methods ignore the influence of high speeds and low-adhesion roads on curved path tracking.

Road adhesion coefficient plays an important role in vehicle electronic control systems. Accurate road adhesion coefficient estimation is critical to improve the path tracking performance of autonomous vehicles. In recent years, to estimate accurate road adhesion coefficient, scholars have proposed various estimation methods. Hahn et al. [9] reported a road friction coefficient estimation algorithm based on a differential global positioning system (DGPS). Wenzel et al. [10] proposed an estimation method based on a double extended Kalman filter (DEKF). Enisz et al. [11] used an extended Kalman filter (EKF) method to estimate the

instantaneous and maximum values of road friction coefficient. Zhao et al. [12] designed an EKF method based on a braking dynamics model considering the load transfer of front and rear axles.

For steering on a wet and slippery road, when the front-wheel loses most of the lateral force (grip), the vehicle (front-drive) will push ahead or rush out of the runway (understeer); when the rear wheel loses most of the lateral force (grip), the vehicle (rear-drive) will drift out or have a tail flicking (oversteer) [13]. To reduce the understeer and oversteer in path tracking, Hang and Chen [14] used a path tracking integrated control based on four-wheel steering (4WS) and direct yaw-moment control to improve the path tracking performance of vehicles on low-adhesion roads. It is generally known that the handling stability and driving safety of 4WS vehicles are much higher than those of front-wheel steering (FWS) vehicles [15, 16]. As early as 1986, Sano et al. [17] proposed a speed function and a steering angle function for 4WS vehicles. In a small steering wheel angle range or at high speed, the rear wheels of the 4WS vehicle were steered in the same direction as the front ones. In a large steering wheel angle range or at low speed, the rear wheels of the 4WS vehicle were steered in the opposite direction to the front ones. This greatly improves the handling stability and driving safety of 4WS vehicles. In [18, 19], by setting the zero-sideslip angle of 4WS vehicle, the stability at high speed and the sensitivity at low speed were significantly improved. In a recent study by Liu et al. [20], a feed-forward controller that can adjust the steering sensitivity coefficient of the 4WS vehicle based on zero-sideslip angle according to the steering angular frequency and vehicle speed is proposed, but this controller is not suitable for low-adhesion curved roads.

The rest of this paper is organized as follows. First of all, small turning radius circular bends (single circle center) considering different restrictions on bend quadrant and travel direction are planned by polar coordinate equations in Section 2. Then, in Section 3, an estimator based on the extended Kalman filter for the vehicle state parameter and road adhesion coefficient is designed. To improve the convenience and accuracy of the estimator, we use the combined slip theory, trigonometric function group fitting, and cubic spline interpolation to estimate the longitudinal and lateral forces of the tire model (215/55 R17). Next, in Section 4, a 4WS vehicle based on a MPC feed-back controller is used to improve the curved path tracking performance at high speeds and on low-adhesion roads, and the lateral displacement and yaw angle tracking errors of the 4WS vehicle in path tracking are minimized. Furthermore, CarSim® simulation effects for the optimal preview feed-back and MPC feed-back controllers under different curved paths, vehicle speeds, and road adhesion coefficients are compared in Section 5. Finally, Section 6 presents the conclusions of the work.

2. Circular Bend and Vehicle Model

2.1. Circular Bend. It is necessary for autonomous vehicles to plan a predetermined curved path in curved path tracking [21–25]. The predetermined path (target path) is usually obtained by high-precision vehicle positioning system, combining the global positioning system (GPS) with the inertial navigation system (INS) [26]. In the absence of electronic map (E-map) data, to facilitate calculations and simulations on small turning radius circular bends (single circle center), the circular bends used as target paths can be planned by polar coordinate equations.

A polar coordinate equation can express a circular bend simply and accurately, and the arc length L_0 of the circular bend is defined as follows:

$$L_0 = \theta_0 R, \tag{1}$$

where θ_0 is the maximum radian of the circular bend and R is the turning radius (m).

To plan all forms of circular bends based on the ground inertial coordinate system, we introduce constraints on bend quadrant and travel direction. The equations of the radian with respect to t for the circular bends under different restrictions are described as follows.

(1) Travel clockwise:

$$\begin{cases} \theta_i = \dfrac{\pi}{2} - \dfrac{u_c t}{R}, & i = 1, \\ \theta_i = -\dfrac{u_c t}{R}, & i = 2, \\ \theta_i = -\dfrac{\pi}{2} - \dfrac{u_c t}{R}, & i = 3, \\ \theta_i = \pi - \dfrac{u_c t}{R}, & i = 4. \end{cases} \tag{2}$$

(2) Travel anticlockwise:

$$\begin{cases} \theta_i = \dfrac{u_c t}{R}, & i = 1, \\ \theta_i = -\dfrac{\pi}{2} + \dfrac{u_c t}{R}, & i = 2, \\ \theta_i = \pi + \dfrac{u_c t}{R}, & i = 3, \\ \theta_i = \dfrac{\pi}{2} + \dfrac{u_c t}{R}, & i = 4, \end{cases} \tag{3}$$

where t is the driving time; θ_i is the radian value corresponding to time t; u_c represents the longitudinal speed based on vehicle coordinate system; $i = 1$ is the first quadrant; $i = 2$ is the second quadrant; $i = 3$ is the third quadrant; and $i = 4$ is the fourth quadrant. Then, the coordinate equations for the circular bends are expressed as follows:

$$\begin{cases} X_d = X_0 + R\cos(\theta_i), \\ Y_d = Y_0 + R\sin(\theta_i), \end{cases} \tag{4}$$

where (X_0, Y_0) is the circle center coordinate; Y_d is the desired lateral displacement based on the ground inertial coordinate system; and X_d is the desired longitudinal displacement based on the ground inertial coordinate system.

After the derivative of the function of Y_d with respect to X_d, the function of the desired yaw angle Ω_d with respect to X_d is expressed as follows:

$$\Omega_d(X_d) = \arctan\left(Y_d'(X_d)\right), \tag{5}$$

where Ω_d represents the desired yaw angle based on the ground inertial coordinate system.

After the derivative of the function of Ω_d with respect to t, the function of the desired yaw rate r_d with respect to t is formulated as follows:

$$r_d(t) = \Omega_d'(t). \tag{6}$$

Taking the restriction of traveling clockwise as an example, Figure 1 shows the right-angle circular bends under four different quadrants, where α is the corner angle and $0 \le \alpha \le 180$ (deg).

Taking the restrictions of traveling anticlockwise and the second quadrant ($i = 2$) as an example, Figure 2 shows the four circular bend diagrams with acute, right, obtuse, and U-shaped angles that meet the restrictions.

Finally, the target paths can be converted into the desired front and rear wheel steering angles and used as initial inputs of autonomous vehicles. For a 4WS vehicle, the yaw rate response is generally set to a first-order lag response and the sideslip angle response is generally set to 0 [27–31]. Its initial inputs can be formulated as follows:

$$\begin{cases} \dfrac{\delta_{fd}(s)}{\delta_{sw}(s)} = \dfrac{I_z s + mbu_c + \left(laC_{af}/u_c\right)}{lC_{af}} \cdot \dfrac{G_{rd}}{1 + T_r s}, \\ \dfrac{\delta_{rd}(s)}{\delta_{sw}(s)} = -\dfrac{I_z s - mau_c + \left(lbC_{ar}/u_c\right)}{lC_{ar}} \cdot \dfrac{G_{rd}}{1 + T_r s}, \end{cases} \tag{7}$$

where s is a Laplace operator; $\delta_{sw} = r_d/G_{rd}$; G_{rd} is the desired steering sensitivity coefficient and $G_{rd} = u_c/(i_0 l + i_0 l K u_c^2)$; K is the stability factor and $K = m(bC_{ar} - aC_{af})/(l^2 C_{af} C_{ar})$; δ_{fd} and δ_{rd} are initial inputs of front and rear wheel steering angles for 4WS vehicles, respectively; and $T_r = 1/\sqrt{((l^2 C_{af} C_{ar}(1 + Ku_c^2))/(u_c^2 m I_z))}$.

2.2. Vehicle Model. A vehicle model (D-class Sedan) of CarSim® is used in the following simulations. The vehicle model is front-drive (Generic 200 KW powertrain with an automatic transmission). A tire model (215/55 R17) used in the vehicle model is a standard lookup table tire model. The main parameters for the vehicle model are shown in Table 1.

3. Estimator Based on EKF

3.1. Vehicle State Parameter Estimation. Ignoring the effects of the suspension system, road roughness, and air resistance, a three-degree-of-freedom (3DOF) vehicle dynamics model considering lateral, longitudinal, and yaw motions is used to estimate the longitudinal speed, sideslip angle, and yaw rate of vehicles [32]. The state space equation of the vehicle dynamics model is shown as follows:

$$\begin{cases} \dot{r} = -\dfrac{a^2 C_{af} + b^2 C_{ar}}{I_z u_c} r - \dfrac{aC_{af} - bC_{ar}}{I_z}\beta + \dfrac{aC_{af}}{I_z}\delta_f, \\ \dot{\beta} = \left(\dfrac{bC_{ar} - aC_{af}}{I_z} - 1\right) r - \dfrac{C_{af} + C_{ar}}{mu_c}\beta + \dfrac{C_{af}}{mu_c}\delta_f, \\ \dot{u}_c = r\beta u_c + a_x. \end{cases} \tag{8}$$

The measurement equation of the vehicle model is shown as follows:

$$a_y = \frac{bC_{ar} - aC_{af}}{mu_c} r - \frac{C_{af} + C_{ar}}{m}\beta + \frac{C_{af}}{m}\delta_f, \tag{9}$$

where δ_f is the front-wheel steering angle, r is the yaw rate based on the vehicle coordinate system, β is the sideslip angle based on the vehicle coordinate system, a_x is the longitudinal acceleration based on the vehicle coordinate system, a_y is the lateral acceleration based on the vehicle coordinate system, the input vector is $u = \begin{bmatrix} \delta_f & a_x \end{bmatrix}^T$, the state vector is $x = \begin{bmatrix} r & \beta & u_c \end{bmatrix}^T$, and the measurement vector is $y = a_y$. After the partial differential of equations (8) and (9) with respect to x, the Jacobian matrices F and H in Figure 3 are calculated as follows:

$$F = \begin{bmatrix} \dfrac{-C_{ar}b^2 - C_{af}a^2}{I_z u_c} & \dfrac{-C_{af}a + bC_{ar}}{I_z} & \dfrac{a^2 C_{af} + b^2 C_{ar}}{I_z u_c^2} r \\ \dfrac{bC_{ar} - aC_{af}}{mu_c^2} - 1 & \dfrac{-C_{af} - C_{ar}}{mu_c} & \dfrac{2(aC_{af} - bC_{ar})r}{mu_c^3} + \dfrac{(C_{af} + C_{ar})\beta - C_{af}\delta_f}{mu_c^2} \\ \beta u_c & r u_c & r\beta \end{bmatrix},$$

$$H = \begin{bmatrix} \dfrac{bC_{ar} - aC_{af}}{mu_c} & \dfrac{-C_{af} - C_{ar}}{m} & \dfrac{aC_{af} - bC_{ar}}{mu_c^2} r \end{bmatrix}. \tag{10}$$

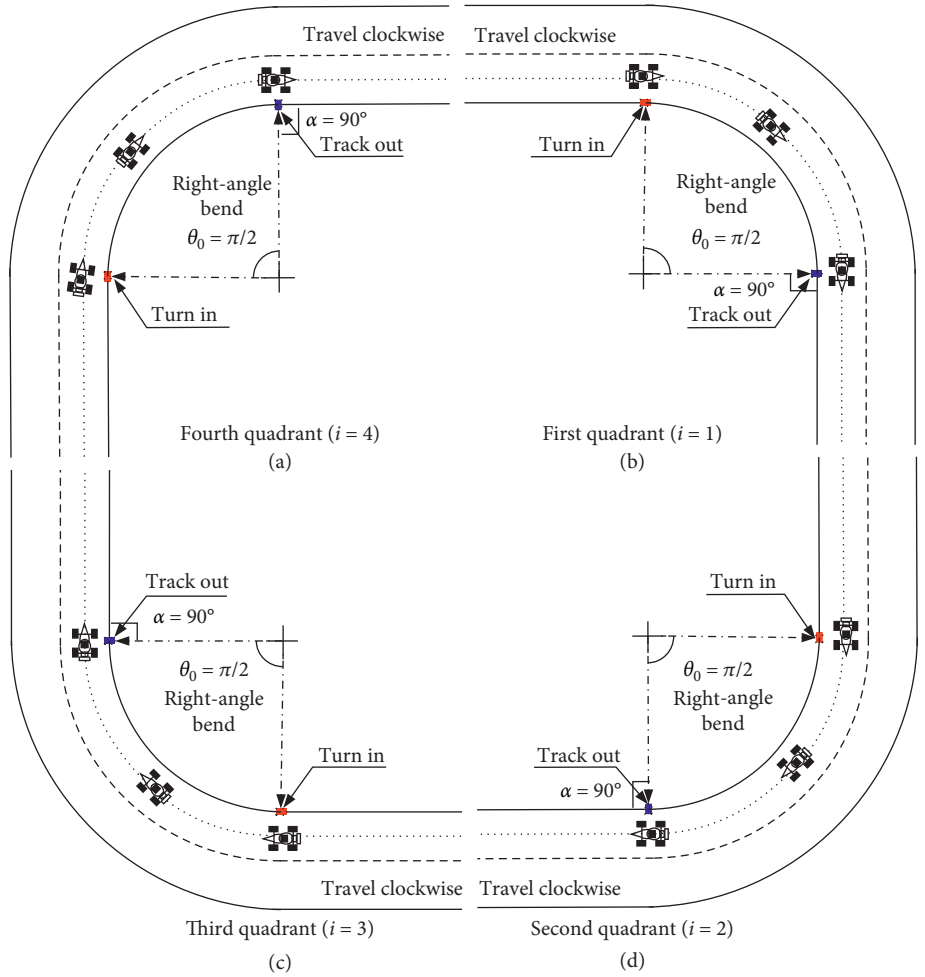

Figure 1: Right-angle circular bends under four different quadrants: (a) fourth quadrant; (b) first quadrant; (c) third quadrant; (d) second quadrant.

Then, the flow chart of EKF algorithm is shown in Figure 3, where $\Phi = e^{F*\Delta t} \approx I + F\Delta t$; $\Delta t = 0.01$ is the sampling time; Q_1 is the covariance matrix of process noise; R_1 is the covariance matrix of measurement noise; f is the state space equation; $\widehat{x}_k$ is the state estimation vector at time k; P_k is the state error covariance matrix at time k; $\widehat{x}_{k-1}$ is the state estimation vector at time $k-1$; and P_{k-1} is the state error covariance matrix at time $k-1$. Given the initial values $\widehat{x}_{k-1}$ and P_{k-1} and $\widehat{x}_k$ and P_k can be updated cyclically. The above estimation process is continually looped until the number of set steps.

3.2. Tire Longitudinal and Lateral Forces Estimation. Professor Pacejka put forward a "magic formula" tire model in 1987, which estimates the tire longitudinal and lateral forces by constructing the trigonometric function group. The tire longitudinal and lateral force estimation equations under a single working condition are shown as follows:

$$\begin{cases} F_{x0} = \mu_0 D_x \sin\left(C_x \arctan\left(B_x\lambda - E_x\left(B_x\lambda - \arctan\left(B_x\lambda\right)\right)\right)\right), \\ F_{y0} = \mu_0 D_y \sin\left(C_y \arctan\left(B_y\beta - E_y\left(B_y\beta - \arctan\left(B_y\beta\right)\right)\right)\right), \end{cases} \tag{11}$$

where $\mu_0 = 1$; λ is the slip ratio; B_x and B_y are the stiffness factors of the tire longitudinal and lateral forces, respectively; C_x and C_y are the curve shape factors of the tire longitudinal and lateral forces, respectively; D_x and D_y are the curve peak factors of the tire longitudinal and lateral forces, respectively; and E_x and E_y are the curvature factors at the curve peak of the tire longitudinal and lateral forces, respectively. These factors are represented by equations containing several different coefficients [33].

Although the "magic formula" has a high fitting accuracy for the tire longitudinal and lateral forces, these coefficients in the above factors are difficult to fit [34, 35]. In order to estimate the longitudinal and lateral forces of the tire model (215/55 R17) conveniently and accurately, we use the combined slip theory, trigonometric function group fitting, and cubic spline interpolation to estimate longitudinal and lateral forces of the tire model.

Firstly, combined with the longitudinal and lateral force tabular data of the tire model (the tabular data are measured on a laboratory or on-road tester, and they are all measured under the condition that the road adhesion coefficient μ is 1), tabular data under 10 different tire loads are selected, which are represented by the purple, pink, green, cyan, and blue

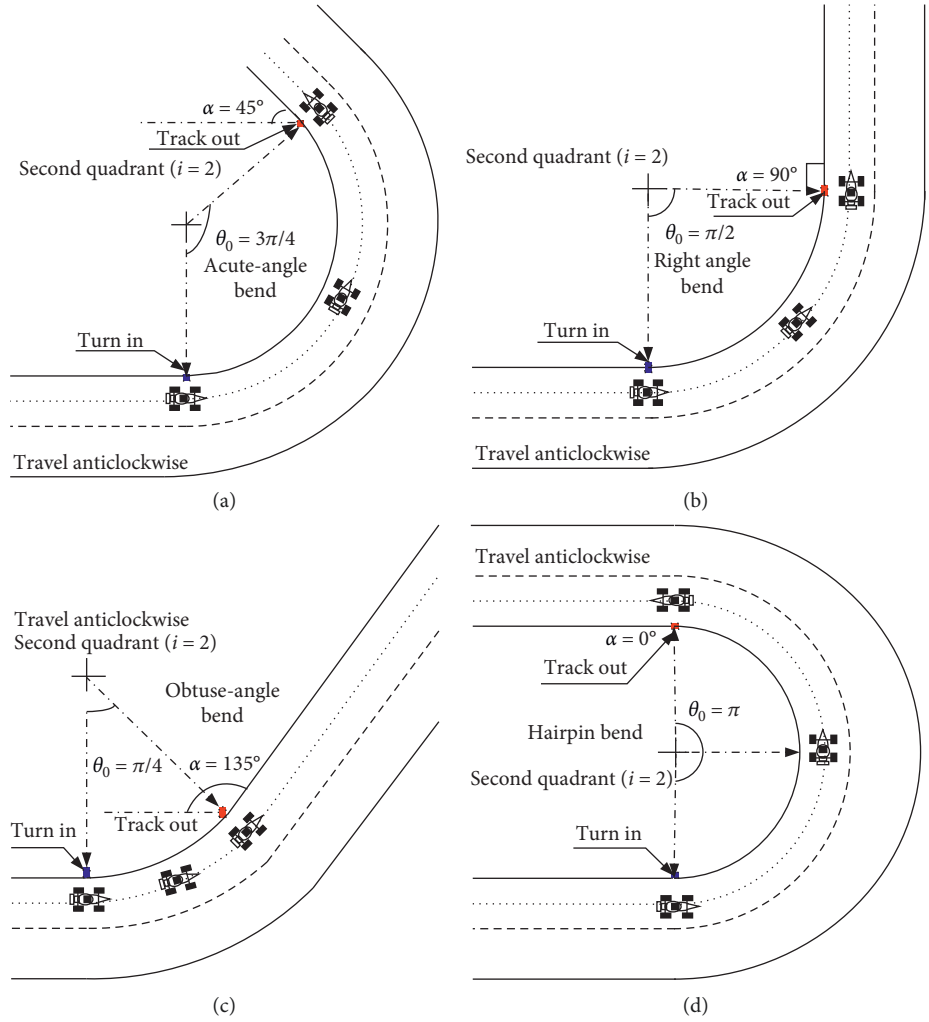

FIGURE 2: Four circular bend diagrams under the restrictions of travel anticlockwise and second quadrant ($i = 2$): (a) acute angle; (b) right angle; (c) obtuse angle; (d) U-shaped angle.

lines in Figure 4. Using the trigonometric function group to fit these tabular data, the fitting results are represented by the five types of black lines in Figure 4. These factors after fitting are shown as follows (RMSE is the root mean square error):

(1) Tire load 1725: B_{y1} is 9.342; C_{y1} is 2.753; D_{y1} is 1891.4; E_{y1} is 1.123; and RMSE is 0.0096

(2) Tire load 3500: B_{y2} is 9.909; C_{y2} is 2.694; D_{y2} is 3698.8; E_{y2} is 1.114; and RMSE is 0.0089

(3) Tire load 6100: B_{y3} is 10.17; C_{y3} is 2.626; D_{y3} is 5382.1; E_{y3} is 1.109; and RMSE is 0.0077

(4) Tire load 6950: B_{y4} is 9.943; C_{y4} is 2.573; D_{y4} is 6971.6; E_{y4} is 1.112; and RMSE is 0.0066

(5) Tire load 9005: B_{y5} is 9.029; C_{y5} is 2.565; D_{y5} is 8564.5; E_{y5} is 1.126; and RMSE is 0.0055

(6) Tire load 2105: B_{x1} is 11.37; C_{x1} is 1.528; D_{x1} is 2729.5; E_{x1} is −0.5744; and RMSE is 0.0016

(7) Tire load 3995: B_{x2} is 11.37; C_{x2} is 1.528; D_{x2} is 5459.1; E_{x2} is −0.5744; and RMSE is 0.0016.

(8) Tire load 6120: B_{x3} is 11.37; C_{x3} is 1.528; D_{x3} is 8188.6; E_{x3} is −0.5744; and RMSE is 0.0016

(9) Tire load 7900: B_{x4} is 11.37; C_{x4} is 1.528; D_{x4} is 10918; E_{x4} is −0.5744; and RMSE is 0.0016

(10) Tire load 10100: B_{x5} is 11.37; C_{x5} is 1.528; D_{x5} is 13648; E_{x5} is −0.5745; and RMSE is 0.0016

Secondly, the cubic spline interpolation is used to estimate these factors under other tire loads. Taking the B_y estimation under a certain tire load as an example, the circular calling format of the cubic spline interpolation is shown as follows:

$$y_z = \text{interp1}\left(z_0, y\left(i,:\right), z, \text{“spline”}\right), \tag{12}$$

where $z_0 = [1725, 3500, 6100, 6950, 9005]$; z is a certain tire load; $y\left(i,:\right) = B_{yi}, i = (1{:}\ 5)$; y_z is the interpolation result; and “spline” is the function about cubic spline interpolation. Similarly, the remaining factors can be estimated. Then, the longitudinal force estimation equation (under pure braking/driving conditions) and lateral force estimation equation (under pure steering conditions) under any tire load can be obtained.

Table 1: Parameters of D-class sedan.

Model parameter	Notation	Unit	Value
Yaw moment of inertia	I_z	kg·m^2	4607.47
Vehicle mass	m	kg	1530
Distances from vehicle C.G. to front axle	a	m	1.11
Distances from vehicle C.G. to rear axle	b	m	1.66622
Front-wheel track width	T_{wf}	m	1.55
Rear wheel track width	T_{wr}	m	1.55
Vehicle wheelbase	l	m	2.77622
Vehicle height	h_0	m	1.471
Vehicle length	l_0	m	4.52
Vehicle width	w_0	m	1.8
Cornering stiffness of front axle	C_{af}	N/rad	97937 ∗ 2
Cornering stiffness of rear axle	C_{ar}	N/rad	70287 ∗ 2
Longitudinal stiffness of front axle	C_{lf}	N/rad	85740 ∗ 2
Longitudinal stiffness of rear axle	C_{lr}	N/rad	57110 ∗ 2
Initial transmission ratio of δ_{sw} to δ_f	i_0		23
Front-wheel optimal slip ratio	s_f		0.2
Rear wheel optimal slip ratio	s_r		0.2

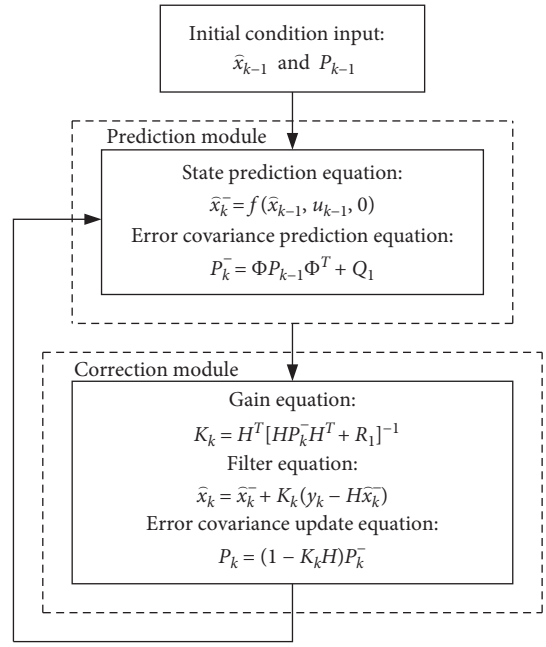

Figure 3: Flow chart of EKF algorithm.

Finally, using the combined slip theory [36, 37], the tire longitudinal and lateral forces under joint conditions can be described as follows:

$$\begin{cases} F_{xij} = \mu_0 F_{x0}(F_z, \lambda) \cdot \dfrac{|\sigma_x|}{\sigma}, \\ F_{yij} = \mu_0 F_{y0}(F_z, \beta) \cdot \dfrac{|\sigma_y|}{\sigma}, \end{cases} \tag{13}$$

where $\mu_0 = 1$; $\sigma_x = -(\lambda/1+\lambda)$; $\sigma_y = -(\tan\beta/1+\lambda)$; $\sigma = \sqrt{\sigma_x^2 + \sigma_y^2}$; F_z is the tire load; $i = f, r$; $j = l, r$; F_{xfl}, F_{xrl}, F_{xfr}, and F_{xrr} are the left front, left rear, right front, and right rear wheel longitudinal forces under joint conditions, respectively; and F_{yfl}, F_{yrl}, F_{yfr}, and F_{yrr} are the left front, left rear, right front, and right rear wheel lateral forces under joint conditions, respectively.

3.3. Road Adhesion Coefficient Estimation. A 3DOF vehicle dynamics model involving tire lateral and longitudinal forces under joint conditions is used to estimate the road adhesion coefficient [38]. The state space equation of the vehicle dynamics model is shown as follows:

$$\begin{cases} a_y = \dfrac{\left(u_{fl}\left(F_{xfl}\delta_f + F_{yfl}\right) + u_{fr}\left(F_{xfr}\delta_f + F_{yfr}\right) + \mu_{rl}F_{yrl} + \mu_{rr}F_{yrr}\right)}{m}, \\ a_x = \dfrac{\left(\mu_{fl}\left(F_{xfl} - F_{yfl}\delta_f\right) + \mu_{fr}\left(F_{xfr} - F_{yfr}\delta_f\right) + \mu_{rl}F_{xrl} + \mu_{rr}F_{xrr}\right)}{m}, \\ \dot{r} = \left(\dfrac{\left(u_{fl}\left(\left(a\left(F_{xfl}\delta_f + F_{yfl}\right) + T_{wf}\right)/\left(2\left(-F_{xfl} + F_{yfl}\delta_f\right)\right)\right) + u_{fr}\left(\left(a\left(F_{xfr}\delta_f + F_{yfr}\right) + T_{wf}\right)/\left(2\left(F_{xfr} - F_{yfr}\delta_f\right)\right)\right) + u_{rl}\left(\left(-bF_{yrl} - T_{wr}\right)/(2F_{xrl})\right) + u_{rr}\left(\left(-bF_{yrr} + T_{wr}\right)/(2F_{xrr})\right)}{I_z}\right), \end{cases} \tag{14}$$

where the input vector $u = \left[\delta_f \;\; F_{xfl} \;\; F_{xfr} \;\; F_{xrl} \;\; F_{xrr} \;\; F_{yfl} \;\; F_{yfr} F_{yrl}\right]^T$; the state vector $x = \left[\mu_{fl} \;\; \mu_{fr} \;\; \mu_{rl} \;\; \mu_{rr}\right]^T$, μ_{fl}, μ_{fr}, μ_{rl}, and μ_{rr} are the left front, right front, left rear, and right rear wheel adhesion coefficients, respectively; and the measurement vector $y = \left[a_x \;\; a_y \;\; \dot{r}\right]^T$. After the partial differential of equation (14) with respect to x, the Jacobian matrices F and H in Figure 3 are calculated as follows:

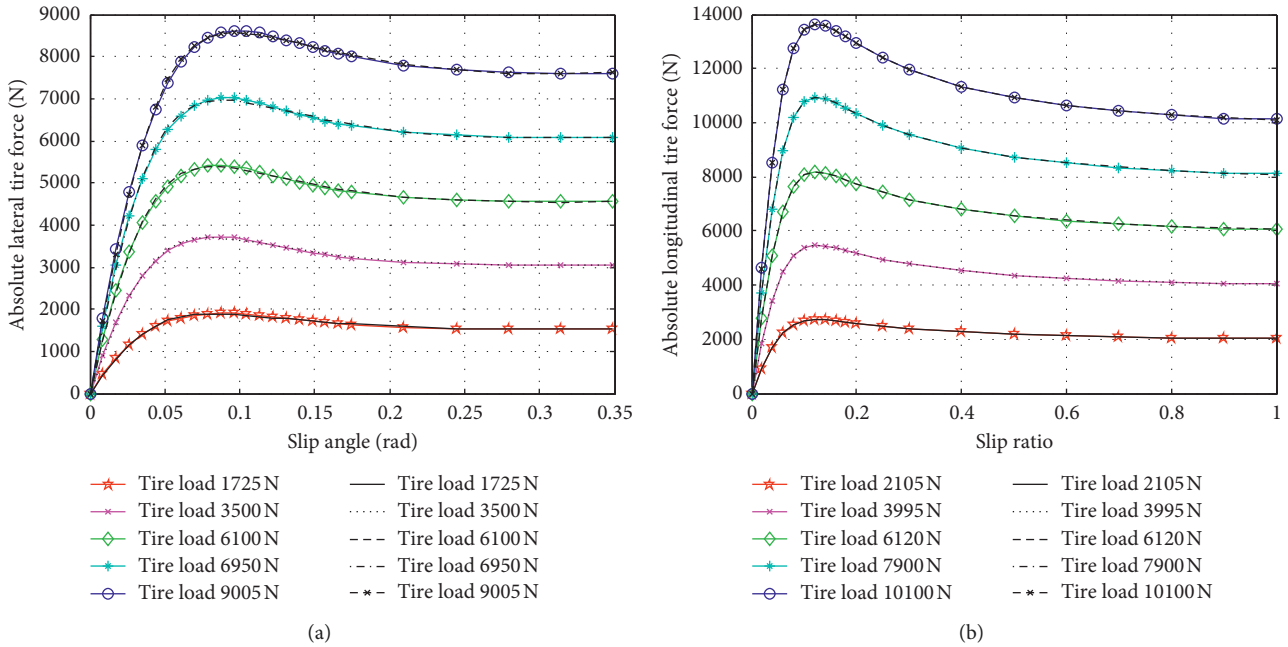

FIGURE 4: Longitudinal and lateral force tabular data under $\mu = 1$: (a) the lateral tire forces under pure steering conditions; (b) the longitudinal tire forces under pure driving/braking conditions.

$$F = \begin{bmatrix} 1 & 0 & 0 & 0 \\ 0 & 1 & 0 & 0 \\ 0 & 0 & 1 & 0 \\ 0 & 0 & 0 & 1 \end{bmatrix},$$

$$H = \begin{bmatrix} \dfrac{F_{xfl} - F_{yfl}\delta_f}{m} & \dfrac{F_{xfr} - F_{yfr}\delta_f}{m} & \dfrac{F_{xrl}}{m} & \dfrac{F_{xrr}}{m} \\ F_{xfl}\delta_f + F_{yfl} & F_{xfr}\delta_f + F_{yfr} & F_{yrl} & F_{yrr} \\ H(3,1) & H(3,2) & H(3,3) & H(3,4) \end{bmatrix},$$

$$H(3,1) = \frac{\left(a\left(F_{xfl}\delta_f + F_{yfl}\right) + T_{wf}\left(-F_{xfl} + F_{yfl}\delta_f\right)/2\right)}{I_z},$$

$$H(3,3) = \frac{\left(-bF_{yrl} - T_{wr}F_{xrl}/2\right)}{I_z},$$

$$H(3,2) = \frac{\left(a\left(F_{xfr}\delta_f + F_{yfr}\right) + T_{wf}\left(F_{xfr} - F_{yfr}\delta_f\right)/2\right)}{I_z},$$

$$H(3,4) = \frac{\left(-bF_{yrr} + T_{wr}F_{xrr}/2\right)}{I_z}. \tag{15}$$

The flow chart of the road adhesion coefficient estimation algorithm is similar to that of the vehicle state parameter estimation, as shown in Figure 3.

3.4. Verification of the Estimator. The overall block diagram of the estimator for vehicle state parameter and road adhesion coefficient is shown in Figure 5.

A joint adhesion road is used in the verification. The features of the joint adhesion road are detailed as follows: a road of a total length of about 321 m, with the first 28 m a high-μ section (a road adhesion coefficient of 0.85), and the rest a low-μ section (a road adhesion coefficient of 0.5). In addition, a two-way single-lane road is used in the estimation, and it is a right-angled circular bend (the corner angle α is 90 deg), as shown in Figure 6(a), where the width of each lane is 6 m, the blue dashed line is the target path, and the turning radius is 37.5 m. The estimated road adhesion coefficient and vehicle state parameters at $u_c = 50$ km/h are shown in Figures 6(b)–6(e), where a uniformly distributed random signal (the minimum value is 0 and the maximum value is 0.02) is added to the actual outputs of CarSim® vehicle considering uncertain disturbances. The parameter settings of vehicle state parameter estimation are shown as follows: $Q_1 = I_{3\times3}$; $\widehat{x}_{k-1} = [\,0 \;\; 0 \;\; 50/3.6\,]$; $P_{k-1} = I_{3\times3}$; $R_1 = 0.01$; and P_k can be updated cyclically in the form of 3×3 matrix. The parameter settings of road adhesion coefficient estimation are shown as follows: $Q_1 = I_{4\times4}$; $\widehat{x}_{k-1} = [\,0.5 \;\; 0.5 \;\; 0.5 \;\; 0.5\,]$; $P_{k-1} = I_{4\times4}$; $R_1 = I_{3\times3}$; and P_k can be updated cyclically in the form of 4×4 matrix. Figure 6 shows that even in the case of a small turning radius and low-adhesion road, the estimator can quickly and accurately estimate the vehicle state parameters and road adhesion coefficient.

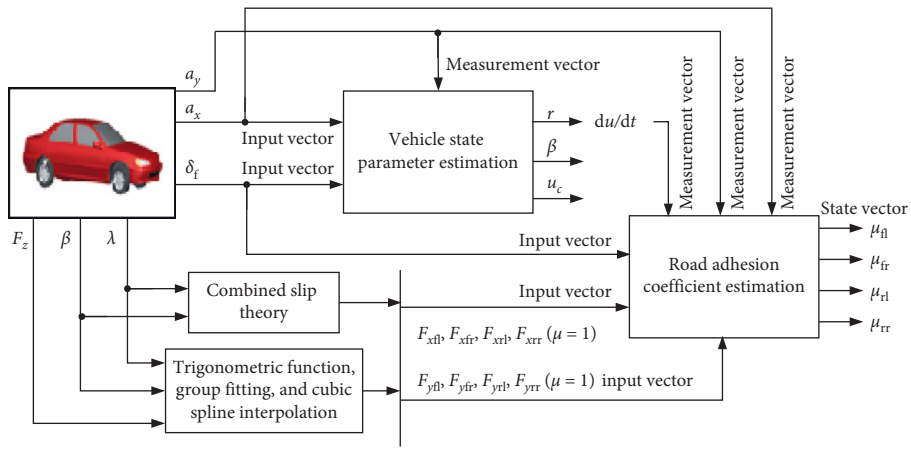

Figure 5: Overall block diagram of the estimator.

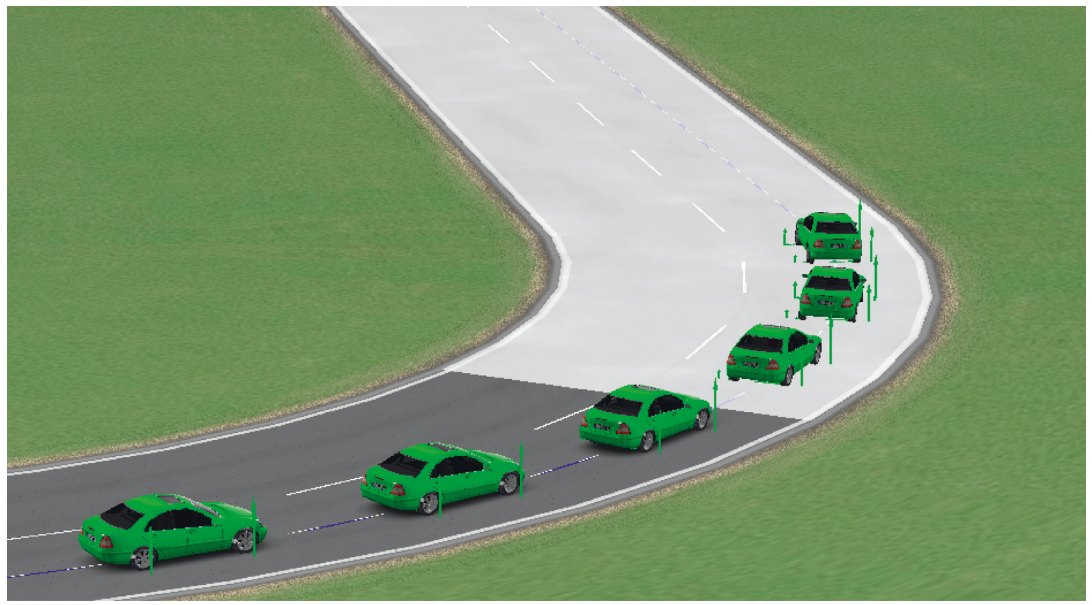

(a)

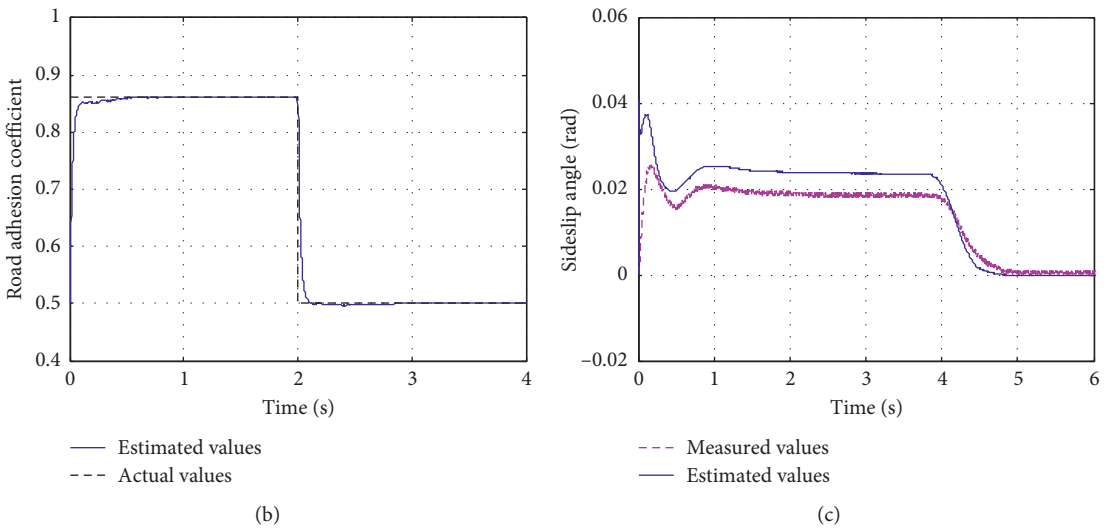

(b) (c)

Figure 6: Continued.

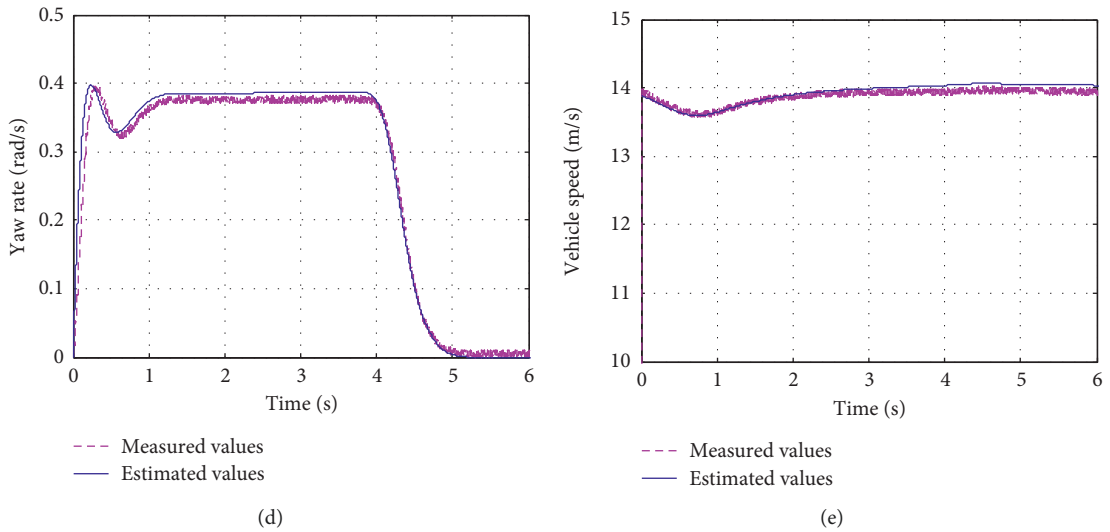

Figure 6: Estimation results: (a) animation effect; (b) road adhesion coefficient; (c) sideslip angle; (d) yaw rate; (e) vehicle speed.

4. MPC Feed-Back Controller

MPC generally includes predictive model, rolling optimization, and feed-back correction. It mainly compensates for system errors through feed-back correction and compensates for the effects caused by time variance and interference through rolling optimization [39, 40]. Since the effects of the tire nonlinearity, tire load transfer, road low-adhesion, and crosswind, the actual trajectories often deviate from the desired trajectories in path tracking [20]. To minimize these deviations, a MPC feed-back controller is used to follow the desired lateral displacement and the desired yaw angle and minimize the tracking errors between the desired values and the actual values. First, a nonlinear dynamic model considering the transformation between the vehicle coordinate system and the ground inertial coordinate system is described as follows:

$$\begin{cases} \dot{v}_y = \dfrac{-(C_{af}+C_{ar})}{mu_c}v_y + \left(\dfrac{bC_{ar}-aC_{af}}{mu_c} - u_c\right)r + \dfrac{C_{af}}{m}\delta_f + \dfrac{C_{ar}}{m}\delta_r + \dfrac{C_{lf}s_f}{m}\delta_f + \dfrac{C_{lr}s_r}{m}\delta_r, \\ \dot{r} = \dfrac{aC_{lf}s_f}{I_z}\delta_f - \dfrac{bC_{lr}s_r}{I_z}\delta_r - \dfrac{C_{af}a^2 + C_{ar}b^2}{I_z u_c}r + \dfrac{bC_{ar}-aC_{af}}{I_z u_c}v_y + \dfrac{aC_{af}}{I_z}\delta_f - \dfrac{bC_{ar}}{I_z}\delta_r, \\ \dot{u}_c = v_y r + \dfrac{C_{lf}s_f}{m} + \dfrac{C_{lr}s_r}{m} + \dfrac{C_{af}\left(\left(v_y + \mathrm{ar}/u_c\right) - \delta_f\right)}{m}\delta_f + \dfrac{C_{ar}\left(\left(\left(v_y - br\right)/u_c\right) - \delta_r\right)}{m}\delta_r, \\ \dot{Y} = u_c \sin\Omega + v_y \cos\Omega, \\ \dot{X} = u_c \cos\Omega - v_y \sin\Omega, \end{cases} \tag{16}$$

where δ_r is the rear-wheel steering angle; v_y is the lateral speed based on the vehicle coordinate system; $\dot{Y}$ is the lateral speed based on the ground inertial coordinate system; $\dot{X}$ is the longitudinal speed based on the ground inertial coordinate system; and Ω is the yaw angle based on the ground inertial coordinate system. Then, it is transformed into

$$\dot{\tilde{x}} = A\tilde{x} + B\tilde{u}, \tag{17}$$

where

$$\widetilde{x} = x - x_{\mathrm{d}},$$

$$\widetilde{u} = u - u_{\mathrm{d}},$$

$$u = \delta_{\mathrm{f}},$$

$$u_d = \delta_{\mathrm{fd}},$$

$$x = \left[\begin{array}{cccccc} v_y & u_c & \Omega & r & Y & X \end{array}\right]^{\mathrm{T}},$$

$$x_d = \left[\begin{array}{cccccc} v_{y\mathrm{d}} & u_{c\mathrm{d}} & \Omega_{\mathrm{d}} & r_{\mathrm{d}} & Y_{\mathrm{d}} & X_{\mathrm{d}} \end{array}\right]^{\mathrm{T}},$$

$$A = \left[\begin{array}{cccccc} \dfrac{-(C_{\mathrm{af}} + C_{\mathrm{ar}})}{mu_c} & \dfrac{\partial f_{v_y}}{\partial u_c} & 0 & \dfrac{bC_{\mathrm{ar}} - aC_{\mathrm{af}}}{mu_c} - u_c & 0 & 0 \\ r + \dfrac{C_{\mathrm{af}}\delta_{f,t-1}}{mu_c} + \dfrac{C_{\mathrm{ar}}\delta_{r,t-1}}{mu_c} & \dfrac{\partial f_{u_c}}{\partial u_c} & 0 & v_y + \dfrac{C_{\mathrm{af}}a\delta_{f,t-1}}{mu_c} - \dfrac{C_{\mathrm{ar}}b\delta_{r,t-1}}{mu_c} & 0 & 0 \\ 0 & 0 & 0 & 1 & 0 & 0 \\ \dfrac{bC_{\mathrm{ar}} - aC_{\mathrm{af}}}{I_z u_c} & \dfrac{\partial f_r}{\partial u_c} & 0 & \dfrac{-(C_{\mathrm{af}}a^2 + C_{\mathrm{ar}}b^2)}{I_z u_c} & 0 & 0 \\ \cos(\Omega) & \sin(\Omega) & u_c\cos(\Omega) - v_y\sin(\Omega) & 0 & 0 & 0 \\ -\sin(\Omega) & \cos(\Omega) & -v_y\cos(\Omega) - u_c\sin(\Omega) & 0 & 0 & 0 \end{array}\right], \tag{18}$$

$$B = \left[\begin{array}{c} \dfrac{C_{\mathrm{af}}}{m} + \dfrac{C_{\mathrm{lf}}s_{\mathrm{f}}}{m} \\ \dfrac{-2C_{\mathrm{af}}\delta_{f,t-1} + C_{\mathrm{af}}\left(\left(v_y + \mathrm{ar}\right)/u_c\right)}{m} \\ 0 \\ \dfrac{aC_{\mathrm{lf}}s_{\mathrm{f}}}{I_z} + \dfrac{aC_{\mathrm{af}}}{I_z} \\ 0 \\ 0 \end{array}\right],$$

$$\frac{\partial f_{u_c}}{\partial u_c} = -\frac{C_{\mathrm{af}}\delta_{f,t-1}\left(v_y + \mathrm{ar}\right)}{mu_c^2} - \frac{C_{\mathrm{ar}}\delta_{r,t-1}\left(v_y - \mathrm{br}\right)}{mu_c^2},$$

$$\frac{\partial f_{v_y}}{\partial u_c} = \frac{(C_{\mathrm{af}} + C_{\mathrm{ar}})}{mu_c^2}v_y + \frac{aC_{\mathrm{af}} - bC_{\mathrm{ar}}}{mu_c^2}r - r,$$

$$\frac{\partial f_r}{\partial u_c} = \frac{(C_{\mathrm{af}}a^2 + C_{\mathrm{ar}}b^2)}{I_z u_c^2}r - \frac{bC_{\mathrm{ar}} - aC_{\mathrm{af}}}{I_z u_c^2}v_y.$$

To apply equation (17) to the MPC system, it is discretized as follows:

$$\begin{cases} \widetilde{x}(k+1) = A(k)\widetilde{x}(k) + B(k)\widetilde{u}(k), \\ A(k) = I + TA, \\ B(k) = TB, \end{cases} \tag{19}$$

where T is the sampling time. It is further converted into

$$\begin{cases} \xi(k+1) = \widetilde{A}\xi(k) + \widetilde{B}\Delta\widetilde{u}(k), \\ \eta(k) = \widetilde{C}\xi(k), \end{cases} \tag{20}$$

where the state vector $\xi(k) = \begin{bmatrix} \widetilde{x}(k) \\ \widetilde{u}(k-1) \end{bmatrix}$; the input vector $\Delta\widetilde{u}(k) = \widetilde{u}(k) - \widetilde{u}(k-1)$; the output vector $\eta = \begin{bmatrix} X & Y \end{bmatrix}^T$; $\widetilde{A} = \begin{bmatrix} A_{n\times n} & B_{n\times m} \\ 0_{m\times n} & I_{m\times m} \end{bmatrix}$ and $\widetilde{B} = \begin{bmatrix} B_{n\times m} \\ I_{m\times m} \end{bmatrix}$; and n and m are the dimensions of the state vector and output vector, respectively.

Next is a rolling optimization process, we can convert the MPC problem into a quadratic programming problem [41]. Its mathematical model is expressed as follows:

$$\min_{\Delta U,\varepsilon} \quad \frac{1}{2}\begin{bmatrix} \Delta U \\ \varepsilon \end{bmatrix}^T H_2 \begin{bmatrix} \Delta U \\ \varepsilon \end{bmatrix} + f_2^T \begin{bmatrix} \Delta U \\ \varepsilon \end{bmatrix} \tag{21}$$

$$\text{s.t.} \quad \begin{cases} A_{\text{cons}} \begin{bmatrix} \Delta U & \varepsilon \end{bmatrix}^T \le b_{\text{cons}}, \\ lb \le \begin{bmatrix} \Delta U & \varepsilon \end{bmatrix}^T \le ub, \end{cases}$$

where ΔU is the input increment; H_2 is the quadratic matrix of quadratic programming; f_2 is the one item vector of quadratic programming; A_{cons} is the coefficient matrix in linear inequality constraint; b_{cons} is the right-end vector in linear inequality constraint; $lb = \begin{bmatrix} \Delta U_{\min} & 0 \end{bmatrix}^T$; $ub = \begin{bmatrix} \Delta U_{\max} & \varepsilon \end{bmatrix}^T$; and ε is the relaxation factor. Its optimization objective function is set to

$$\begin{aligned} J(\xi(k), \widetilde{u}(k-1), \Delta U(k)) = {} & \sum_{i=1}^{N_p} \left\| \eta(k+i\,|\,k) - \eta_d(k+i\,|\,k) \right\|_{Q_2}^2 \\ & + \sum_{i=1}^{N_c-1} \left\| \Delta\widetilde{u}(k+i\,|\,k) \right\|_{R_2}^2 + \rho\varepsilon^2, \end{aligned} \tag{22}$$

where Q_2 and R_2 are weighting matrices; ρ is the weight coefficient; N_p is the prediction time domain; and N_c is the control time domain.

To avoid a sudden change in the input vector, the problem of constrained optimization for each step is shown as follows [42, 43]:

$$\begin{cases} \min\limits_{\Delta U_t,\varepsilon} J(\xi(k), \widetilde{u}(k-1), \Delta U(k)), \\ \text{s.t.} \quad \Delta\widetilde{u}_{\min}(i+k) \le \Delta\widetilde{u}(i+k) \le \Delta\widetilde{u}_{\max}(i+k), \quad i = 0, 1, \ldots, N_c - 1, \\ \widetilde{u}_{\min}(i+k) \le \widetilde{u}(i+k) \le \widetilde{u}_{\max}(i+k), \quad i = 0, 1, \ldots, N_c - 1, \\ \widetilde{\eta}_{\min}(i+k) - \varepsilon \le \widetilde{\eta}(i+k) \le \widetilde{\eta}_{\max}(i+k) + \varepsilon, \quad i = 0, 1, \ldots, N_c - 1. \end{cases} \tag{23}$$

Calling the quadratic programming function (quadprog), which is expressed as follows:

$$\begin{aligned} & [\Delta U, fval, \text{exitflag}] \\ & = \text{quadprog}(H_2, f_2, A_{\text{cons}}, b_{\text{cons}}, [\,], [\,], lb, ub, \Delta U_0, \text{options}), \end{aligned} \tag{24}$$

where $\Delta U_0 = \text{zeros}(N_c + 1, 1)$ and options = optimset("Algorithm", "active – set").

After solving each control cycle, a series of input increments in the control time domain are obtained:

$$\Delta U = \left[\Delta\widetilde{u}(k\,|\,k), \Delta\widetilde{u}(k+1\,|\,k), \ldots, \Delta\widetilde{u}\left(k + N_c - 1\,\middle|\,k\right) \right]^T. \tag{25}$$

Finally, there is a process of feed-back correction. The first element of the control sequence acts on the MPC system:

$$U_e(k) = u(k) = u(k-1) + \Delta\widetilde{u}(k\,|\,k), \tag{26}$$

where U_e represents the feed-back control (front-wheel steering angle). The above control process is continually looped until path tracking is completed.

5. Curved Path Tracking Simulations

5.1. Two-Path Tracking Controllers. Two-path tracking controllers for autonomous vehicles in the following simulations are shown as follows:

(1) The optimal preview feed-back controller for an FWS autonomous vehicle is defined as controller 1, which is an FWS path tracking controller. CarSim® has its own optimal preview path tracking control model located in "Steering by the Closed-loop Driver Model." The red vehicle in the following simulations represents controller 1.

(2) The MPC feed-back controller for a 4WS autonomous vehicle is defined as controller 2, which is a 4WS path tracking controller. The blue vehicle in the following simulations represents controller 2. The block diagram of controller 2 is shown in Figure 7, where $\delta_f = \delta_{fd} + U_e$ and $\delta_r = \delta_{rd}$.

5.2. Circular Bend Simulations at Low Speeds and on High-Adhesion Roads. For the circular bend simulation, the coordinates (X_d and Y_d) of the target path can be updated continuously by polar coordinate equations depending on R, u_c, α, and (X_0, Y_0) variables.

The target path of this simulation is a right-angled circular bend (travel anticlockwise and second quadrant), which is shown in Figure 2(b) (the corner angle α is 90 deg). A one-way four-lane road is applied to the simulation, where the width of each lane is 3.5 m, the turning radius R is 37.5 m, the initial coordinates of the autonomous vehicle are $(0, 0)$, the ending coordinates of the autonomous vehicle are $(300, 300)$, the circle center coordinates are $(X_0, Y_0) = (262.5, 37.5)$, and the road adhesion coefficient of the dry asphalt road is set to 0.85. The road conditions meet the SAE standards J3087_201710 [44]. The path

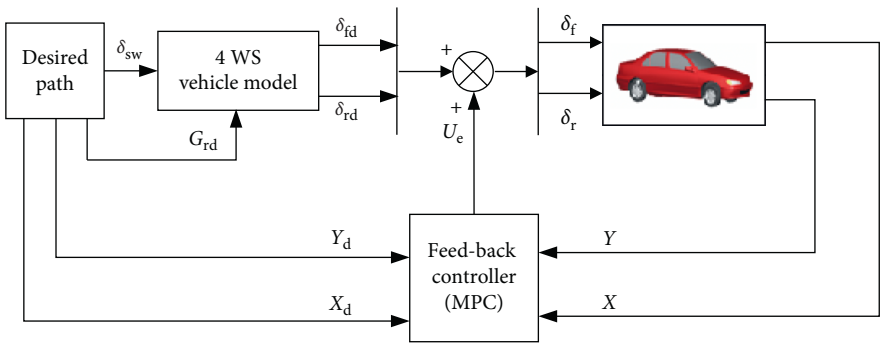

Figure 7: Block diagram of controller 2.

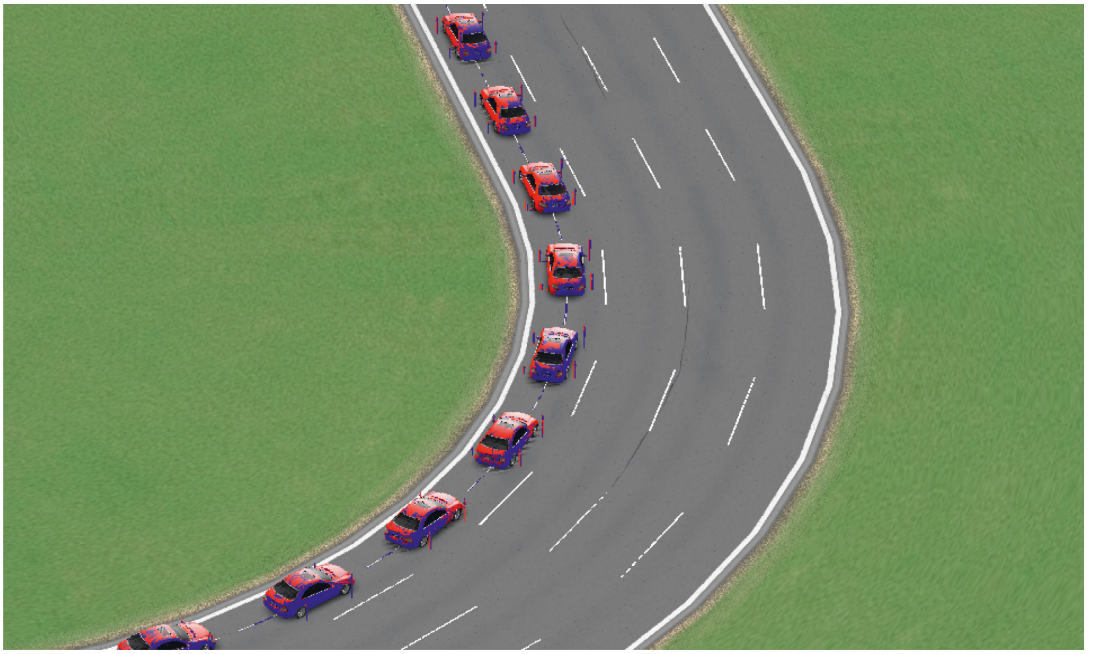

(a)

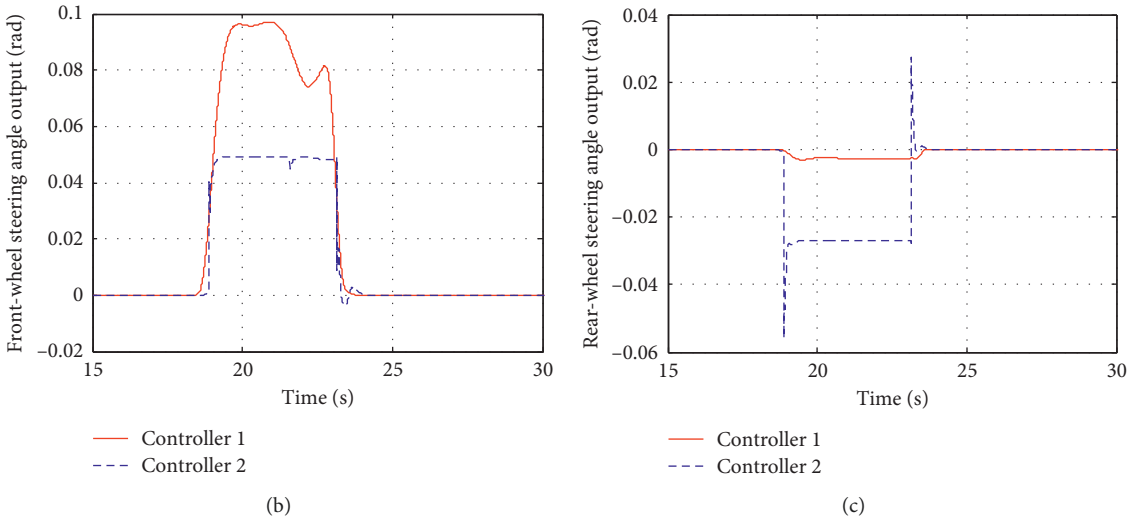

(b)

(c)

Figure 8: Curved path tracking simulation results for red and blue vehicles at u_c = 50 km/h and μ = 0.85: (a) animation effect; (b) front-wheel steering angle; (c) rear-wheel steering angle.

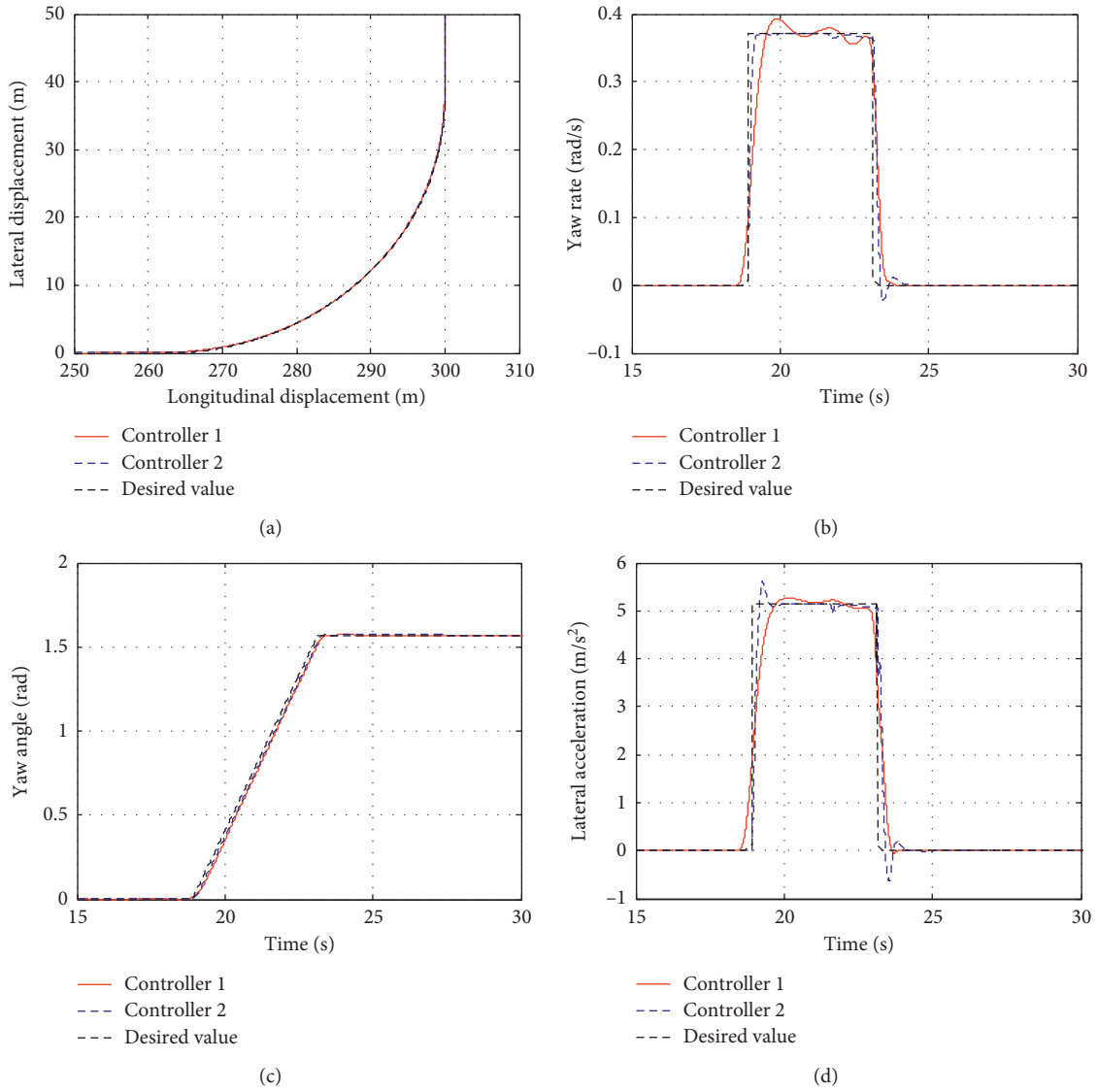

FIGURE 9: Simulation results for red and blue vehicles at $u_c = 50$ km/h and $\mu = 0.85$: (a) Y with respect to X; (b) r with respect to t; (c) Ω with respect to t; (d) a_y with respect to t.

tracking animation effects and steering angles for the red and blue vehicles at $u_c = 50$ km/h and $\mu = 0.85$ are shown in Figure 8. The longitudinal and lateral displacements, lateral accelerations, yaw angles, and yaw rates for the red and blue vehicles at $u_c = 50$ km/h and $\mu = 0.85$ are shown in Figure 9. The detailed constraints of the MPC are shown as follows: the input increment constraints, $-1\,\text{rad/s} \le \Delta u = \Delta\delta_f \le 1\,\text{rad/s}$; the input vector constraints, $-0.25\,\text{rad} \le u = \delta_f \le 0.25\,\text{rad}$; the output vector constraints: $\begin{bmatrix} 0\,\text{m} \\ 0\,\text{m} \end{bmatrix} \le \eta = \begin{bmatrix} X \\ Y \end{bmatrix} \le \begin{bmatrix} 300\,\text{m} \\ 300\,\text{m} \end{bmatrix}$; $Q_2 = \begin{bmatrix} 800 & 0 & 0 \\ 0 & 80 & 0 \\ 0 & 0 & 80 \end{bmatrix}$; $N_p = 30$; $N_c = 10$; $T = 0.01$; $\varepsilon = 1000$; $\rho = 1000$; and $R_2 = 5 * 10^5$. The detailed optimal preview parameter settings are shown as follows: the driver preview time is 0.5 s; the driver time lag is 0 s; the low-speed dynamic limit is 10 km/h; the maximum steering wheel angle is 720 deg; and the maximum steering wheel angle rate is 1200 deg/s.

It can be seen from Figures 8(b) and 8(c) that the red vehicle is an FWS vehicle and the blue vehicle is a 4WS vehicle. Even if the two vehicles have different front and rear wheel steering angles, Figures 9(a) and 9(c) show that they can still achieve effective path tracking without pushing ahead (understeer) or tail flicking (oversteer) at low speeds and on high-adhesion roads. It can be seen that there is little difference in the control effect under steady-state conditions in Figures 9(b) and 9(d).

5.3. Circular Bend Simulations at Low Speeds and on Low-Adhesion Roads. The target path of this simulation is the same as in Section 5.2. The road adhesion coefficient of the wet and slippery road is set to 0.5. The curved path tracking animation effects and steering angles for red and blue

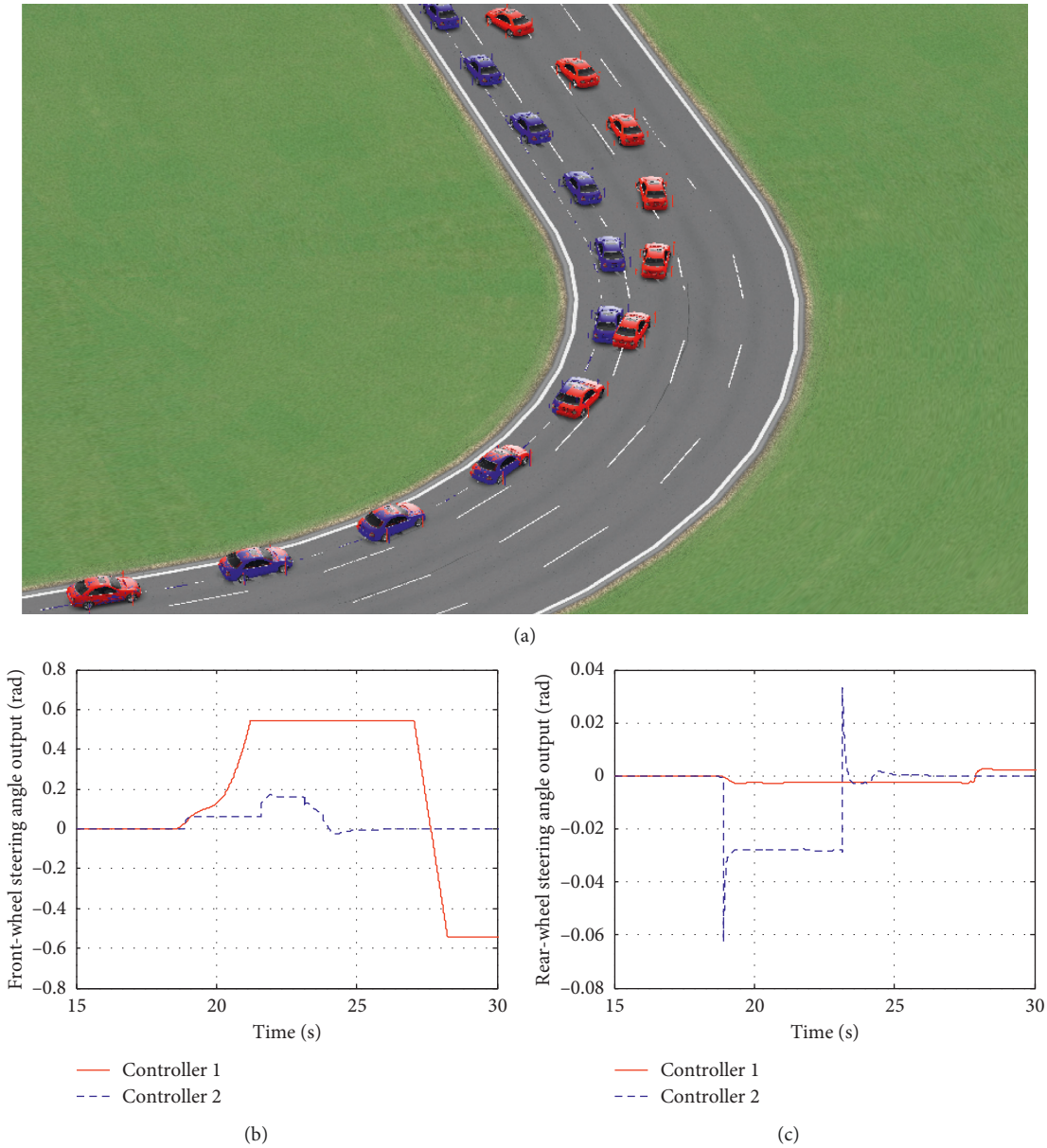

FIGURE 10: Curved path tracking simulation results for red and blue vehicles at $u_c = 50$ km/h and $\mu = 0.5$: (a) animation effect; (b) front-wheel steering angle; (c) rear-wheel steering angle.

vehicles at $u_c = 50$ km/h and $\mu = 0.5$ are shown in Figure 10. The longitudinal and lateral displacements, lateral accelerations, yaw angles, and yaw rates for red and blue vehicles at $u_c = 50$ km/h and $\mu = 0.5$ are shown in Figure 11. The constraints of the MPC and the optimal preview parameter settings are the same as in Section 5.2.

When μ drops to 0.5, Figure 10(a) shows that the red vehicle has obvious sideslip (the maximum deviation is about 4 m). Figure 10(a) shows that the blue vehicle has smaller sideslip (the maximum deviation is about 1 m), and its path tracking performance is significantly better than that of the red vehicle on the low-adhesion road. The reason for this phenomenon is that the rear wheels of the blue vehicle are steered in the opposite direction to the front ones when entering the corner, and its rear wheels are steered in the same direction as the front ones when driving out of the corner, as shown in Figures 10(b) and 10(c). This situation greatly improves the safety and stability of the 4WS vehicle in path tracking on a small turning radius and low-adhesion curved road [45]. Figure 11 shows that the yaw angle, yaw rate, and lateral acceleration values of the blue vehicle are closer to the desired values, and the vehicle maintains good path tracking performance even on low-adhesion roads with small turning radius.

5.4. True Variable Curvature Curved Road Simulations at High Speeds and on Low-Adhesion Roads. For the curved path tracking on real roads, the polar coordinate equation (4) are replaced by the coordinates of the electronic map (E-

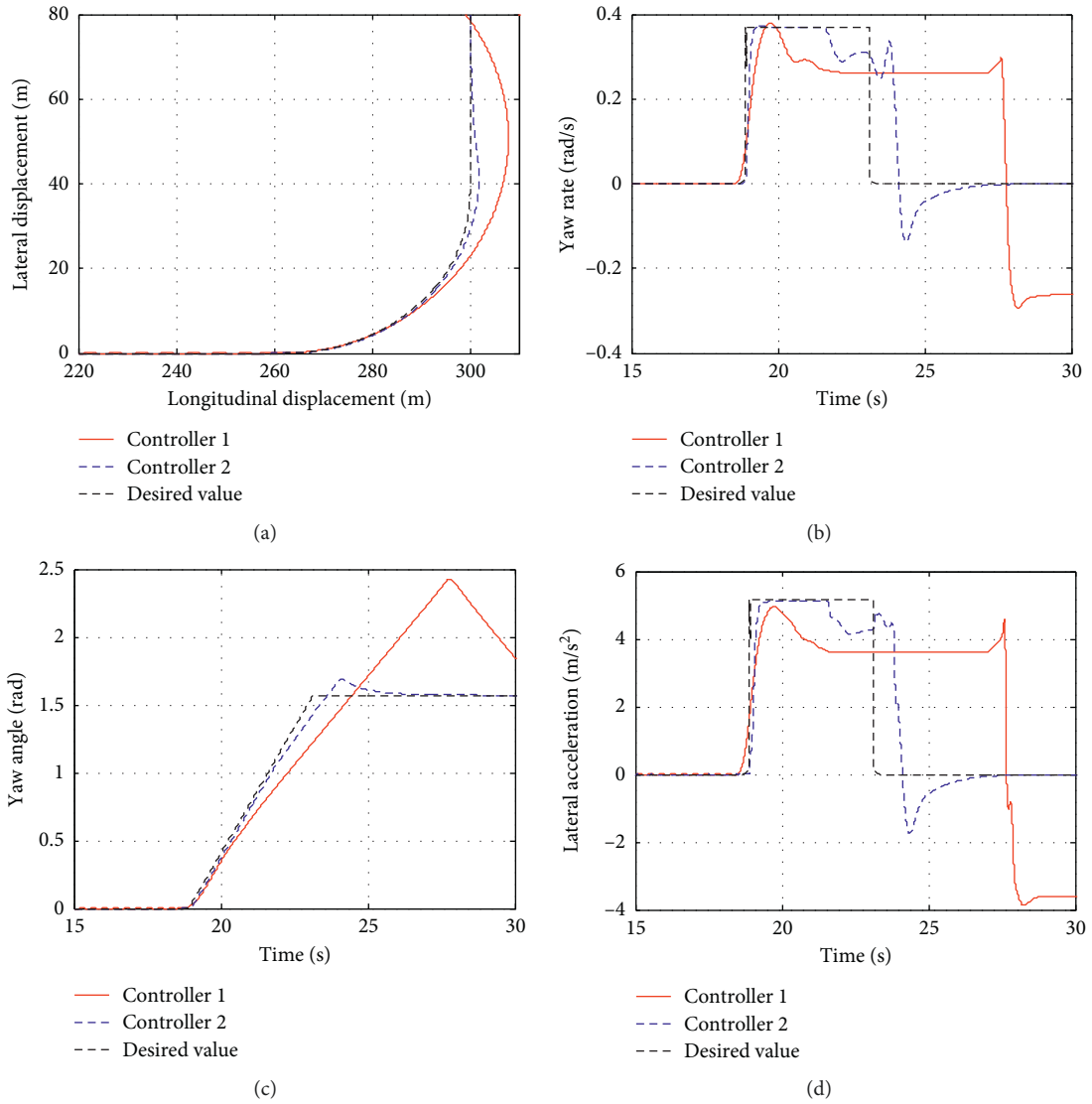

FIGURE 11: Simulation results for red and blue vehicles at $u_c = 50$ km/h and $\mu = 0.5$: (a) Y with respect to X; (b) r with respect to t; (c) Ω with respect to t; (d) a_y with respect to t.

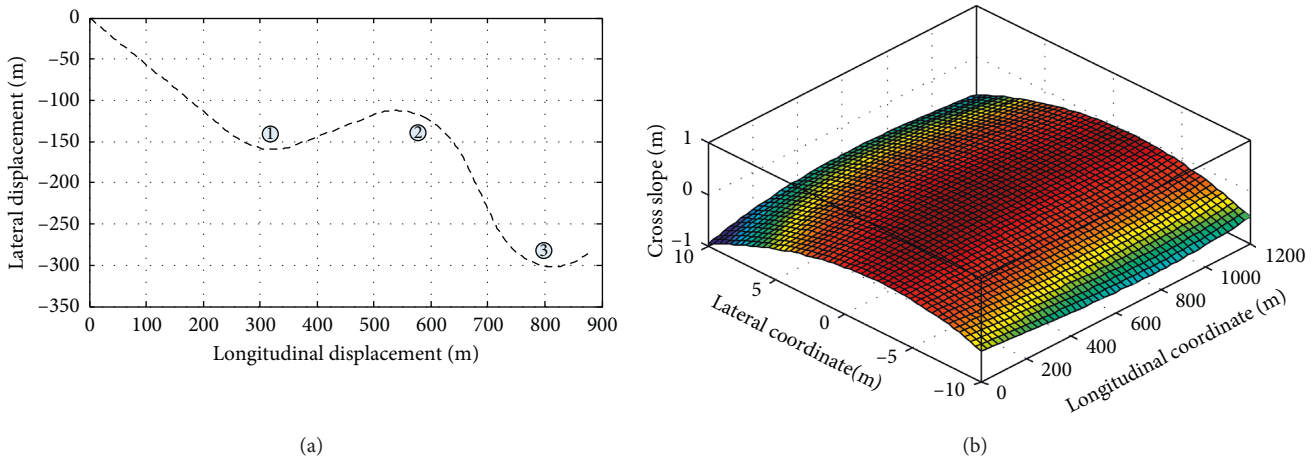

FIGURE 12: True variable curvature curved road: (a) coordinates (X_d, Y_d) and (b) cross slopes.

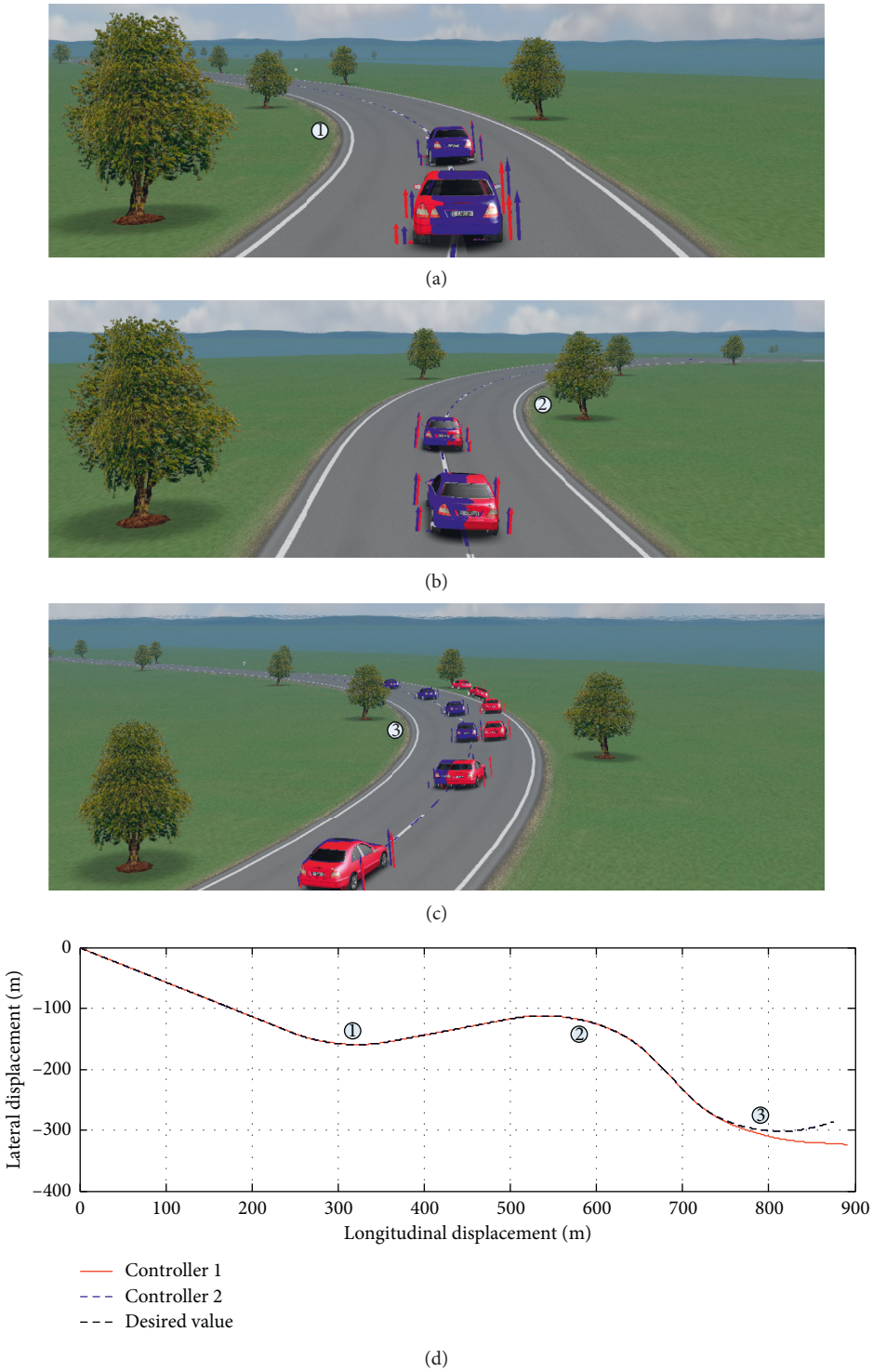

Figure 13: Curved path tracking effects for red and blue vehicles: (a) bend ①; (b) bend ②; (c) bend ③; (d) Y with respect to X.

map), and the coordinates (X_d, Y_d) of the target path can be updated continuously by high-precision vehicle positioning system combining GPS with INS.

A true variable curvature curved road is shown as follows: the road adhesion coefficient of the wet and slippery road is set to 0.5; the minimum turning radius of the bend ① is $R_{min} \approx 167$ m; the minimum turning radius of the bend ② is $R_{min} \approx 143$ m; and the minimum turning radius of the bend ③ is $R_{min} \approx 125$ m. The coordinates (X_d, Y_d) of the true variable curvature curved road are shown in Figure 12(a). The cross slopes of the true variable curvature curved road are shown in Figure 12(b).

The constraints of the MPC are shown as follows: the output vector constraints is $\begin{bmatrix} 0\,\text{m} \\ -350\,\text{m} \end{bmatrix} \leq \eta = \begin{bmatrix} X \\ Y \end{bmatrix} \leq$

$\begin{bmatrix} 900\,\text{m} \\ 0\,\text{m} \end{bmatrix}$, and other constraints are the same as in Section 5.2. The optimal preview parameter settings are the same as in Section 5.2. The curved path tracking effects for red and blue vehicles at $u_c = 100\,\text{km/h}$ and $\mu = 0.5$ are shown in Figure 13. Figure 13 shows that the red vehicle loses control and rushes out of the runway when passing the bend ③, but the blue vehicle maintains good path tracking performance even at high speeds and on low-adhesion roads.

6. Conclusions

The results of this paper can be summarized as follows.

Since the combined slip theory, trigonometric function group fitting, and cubic spline interpolation are used, it is more convenient and accurate in estimating longitudinal and lateral forces and road adhesion coefficients. Compared to the FWS vehicle with an optimal preview path tracking controller, the 4WS vehicle with a MPC path tracking controller can more effectively improve safety and stability at high speeds and on low-adhesion roads. In the future, the path tracking test in the real 4WS autonomous vehicles needs to be implemented and the suspension and braking control systems for 4WS autonomous vehicles in curved path tracking need to be studied further.

Data Availability

The data used to support the findings of this study are included within the article.

Conflicts of Interest

The authors declare no conflicts of interest.

Authors' Contributions

R.L. put forward the original concept, proposed the control strategy, and wrote the article. M.W., J.W., and N.S. gave their valuable suggestions on the research design. Furthermore, R.L., M.W., J.W., and N.S. analyzed and discussed the simulation results.

Acknowledgments

This work was supported by the National Natural Science Foundation of China (Grant no. 51775268), Funding of Jiangsu Innovation Program for Graduate Education (Grant no. KYLX16_0328), and Zhejiang Provincial Public Welfare Technology Application Research Project of China (Grant no. 2017C35011).

References

[1] A. Vahidi and A. Eskandarian, "Research advances in intelligent collision avoidance and adaptive cruise control," *IEEE Transactions on Intelligent Transportation Systems*, vol. 4, no. 3, pp. 143–153, 2003.

[2] C. C. MacAdam, "An optimal preview control for linear systems," *Journal of Dynamic Systems, Measurement, and Control*, vol. 102, no. 3, pp. 188–190, 1980.

[3] C. C. MacAdam, "Application of an optimal preview control for simulation of closed-loop automobile driving," *IEEE Transactions on Systems, Man, and Cybernetics*, vol. 11, no. 6, pp. 393–399, 1981.

[4] Y. Zhu and Ü. Özgüner, "Constrained model predictive control for nonholonomic vehicle regulation problem," *IFAC Proceedings Volumes*, vol. 41, no. 2, pp. 9552–9557, 2008.

[5] F. Borrelli, P. Falcone, T. Keviczky, J. Asgari, and D. Hrovat, "MPC-based approach to active steering for autonomous vehicle systems," *International Journal of Vehicle Autonomous Systems*, vol. 3, no. 2–4, pp. 265–291, 2005.

[6] A. Katriniok and D. Abel, "LTV-MPC approach for lateral vehicle guidance by front steering at the limits of vehicle dynamics," in *Proceedings of the 2011 50th IEEE Conference on Decision and Control and European Control Conference*, pp. 6828–6833, Orlando, FL, USA, December 2011.

[7] E. Kim, J. Kim, and M. Sunwoo, "Model predictive control strategy for smooth path tracking of autonomous vehicles with steering actuator dynamics," *International Journal of Automotive Technology*, vol. 15, no. 7, pp. 1155–1164, 2014.

[8] W. Schwarting, J. Alonso-Mora, L. Paull, S. Karaman, and D. Rus, "Safe nonlinear trajectory generation for parallel autonomy with a dynamic vehicle model," *IEEE Transactions on Intelligent Transportation Systems*, vol. 19, no. 9, pp. 2994–3008, 2017.

[9] J. O. Hahn, R. Rajamani, and L. Alexander, "GPS-based real-time identification of tire-road friction coefficient," *IEEE Transactions on Control Systems Technology*, vol. 10, no. 3, pp. 331–343, 2002.

[10] T. A. Wenzel, K. J. Burnham, M. V. Blundell, and R. A. Williams, "Dual extended Kalman filter for vehicle state and parameter estimation," *Vehicle System Dynamics*, vol. 44, no. 2, pp. 153–171, 2006.

[11] K. Enisz, D. Fodor, I. Szalay, and G. Kohlrusz, "Improvement of active safety systems by the extended Kalman filter based estimation of tire-road friction coefficient," in *Proceedings of the 2014 IEEE International Electric Vehicle Conference (IEVC)*, pp. 1–5, Florence, Italy, December 2014.

[12] Y.-Q. Zhao, H.-Q. Li, F. Lin, J. Wang, and X.-W. Ji, "Estimation of road friction coefficient in different road conditions based on vehicle braking dynamics," *Chinese Journal of Mechanical Engineering*, vol. 30, no. 4, pp. 982–990, 2017.

[13] B. Li and F. Yu, "Design of a vehicle lateral stability control system via a fuzzy logic control approach," *Proceedings of the Institution of Mechanical Engineers, Part D: Journal of Automobile Engineering*, vol. 224, no. 3, pp. 313–326, 2010.

[14] P. Hang and X. Chen, "Integrated chassis control algorithm design for path tracking based on four-wheel steering and direct yaw-moment control," *Proceedings of the Institution of Mechanical Engineers, Part I: Journal of Systems and Control Engineering*, vol. 233, no. 6, pp. 625–641, 2019.

[15] Y. Shibahata, N. Irie, H. Itoh, and K. Nakamura, "The development of an experimental four-wheel-steering vehicle," in *Proceedings of the SAE Technical Paper*, Detroit, MI, USA, December 1986.

[16] Y. Furukawa, N. Yuhara, S. Sano, H. Takeda, and Y. Matsushita, "A review of four-wheel steering studies from the viewpoint of vehicle dynamics and control," *Vehicle System Dynamics*, vol. 18, no. 1–3, pp. 151–186, 1989.

[17] S. Sano, Y. Furukawa, and S. Shiraishi, "Four wheel steering system with rear wheel steer angle controlled as a function of

steering wheel angle," in *Proceedings of the SAE Technical Paper 860625*, Detroit, MI, USA, Febrauary 1986.

[18] P. E. Nikravesh and J. N. Lee, "Optimal four-wheel steering strategy using nonlinear Analytical vehicle models," in *Proceedings of the SAE Technical Paper 931915*, Phoenix, AZ, USA, November 1993.

[19] N. Hamzah, M. K. Aripin, Y. M. Sam, H. Selamat, and M. F. Ismail, "Yaw stability improvement for four-wheel active steering vehicle using sliding mode control," in *Proceedings of the 2012 IEEE 8th International Colloquium on Signal Processing and its Applications*, pp. 127–132, Melaka, Malaysia, March 2012.

[20] R. Liu, M. Wei, and W. Zhao, "Trajectory tracking control of four wheel steering under high speed emergency obstacle avoidance," *International Journal of Vehicle Design*, vol. 77, no. 1-2, pp. 1–21, 2018.

[21] G. Bevan, H. Gollee, and J. O'reilly, "Automatic lateral emergency collision avoidance for a passenger car," *International Journal of Control*, vol. 80, no. 11, pp. 1751–1762, 2007.

[22] W. Nelson, "Continuous-curvature paths for autonomous vehicles," in *Proceedings of the 1989 International Conference on Robotics and Automation*, pp. 1260–1264, Scottsdale, AZ, USA, May 1989.

[23] D. Ren, J. Zhang, J. Zhang, and S. Cui, "Trajectory planning and yaw rate tracking control for lane changing of intelligent vehicle on curved road," *Science China Technological Sciences*, vol. 54, no. 3, pp. 630–642, 2011.

[24] J. Cheng, Y. Zhang, and Z. Wang, "Curve path tracking control for tractor-trailer mobile robot," in *Proceedings of the 2011 Eighth International Conference on Fuzzy Systems and Knowledge Discovery (FSKD)*, pp. 502–506, Shanghai, China, July 2011.

[25] X. Chen, J. Zhang, M. Yang, L. Zhong, and J. Dong, "Continuous-curvature path generation using fermat's spiral for unmanned marine and aerial vehicles," in *Proceedings of the 2018 Chinese Control and Decision Conference (CCDC)*, pp. 4911–4916, Shenyang, China, June 2018.

[26] J. Yang, H. Bao, N. Ma, and Z. Xuan, "An algorithm of curved path tracking with prediction model for autonomous vehicle," in *Proceedings of the 2017 13th International Conference on Computational Intelligence and Security (CIS)*, pp. 405–408, Hong Kong, China, December 2017.

[27] Y. Shan, C. Chen, W. Yang, and B. Li, "Improved path tracking approach for unmanned vehicles based on clothoid curve," in *Proceedings of the 2015 IEEE Intelligent Vehicles Symposium (IV)*, pp. 493–498, Seoul, South Korea, July 2015.

[28] J. Cao, L. Jing, K. Guo, and F. Yu, "Study on integrated control of vehicle yaw and rollover stability using nonlinear prediction model," *Mathematical Problems in Engineering*, vol. 2013, Article ID 643548, 15 pages, 2013.

[29] Y. Wu, L. Wang, and F. Li, "Research on variable steering ratio control strategy of steer-by-wire system," in *Proceedings of the SAE Technical Paper 2018-01-1583*, Kunshan, China, August 2018.

[30] J. Tajima, N. Yuhara, S. Sano, and S. Takimoto, "Effects of steering system characteristics on control performance from the viewpoint of steer-by-wire system design," in *Proceedings of the SAE Technical Paper 1999-01-0821*, Nashville, TN, USA, March 1999.

[31] I. Amdouni, N. Jeddi, and L. El Amraoui, "Optimal control approach developed to four-wheel active steering vehicles," in *Proceedings of the 2013 5th International Conference on Modeling, Simulation and Applied Optimization (ICMSAO)*, pp. 1–6, Hammamet, Tunisia, April 2013.

[32] X. Xue and W. Zhenpo, "Distributed drive electric vehicle state estimation based on extended kalman filter," *Energy Procedia*, vol. 104, pp. 538–543, 2016.

[33] E. Bakker, L. Nyborg, and H. B. Pacejka, "Tyre modelling for use in vehicle dynamics studies (No. 870421)," in *Proceedings of the SAE Technical Paper 870421*, Detroit, MI, USA, February 1987.

[34] W. Liu, H. He, and F. Sun, "Vehicle state estimation based on minimum model error criterion combining with extended Kalman filter," *Journal of the Franklin Institute*, vol. 353, no. 4, pp. 834–856, 2016.

[35] C.-f. Zong, P. Song, and D. Hu, "Estimation of vehicle states and tire-road friction using parallel extended Kalman filtering," *Journal of Zhejiang University-SCIENCE A*, vol. 12, no. 6, pp. 446–452, 2011.

[36] H. B. Pacejka and R. S. Sharp, "Shear force development by pneumatic tyres in steady state conditions: a review of modelling aspects," *Vehicle System Dynamics*, vol. 20, no. 3-4, pp. 121–175, 1991.

[37] H. Pacejka, *Tire and Vehicle Dynamics*, Elsevier, Amsterdam, The Netherlands, 2005.

[38] J. Zhu, Z. Wang, L. Zhang, and W. Zhang, "State and parameter estimation based on a modified particle filter for an in-wheel-motor-drive electric vehicle," *Mechanism and Machine Theory*, vol. 133, pp. 606–624, 2019.

[39] T. Xu and H. Yuan, "Autonomous vehicle active safety system based on path planning and predictive control," in *Proceedings of the 2016 35th Chinese Control Conference (CCC)*, pp. 8889–8895, Chengdu, China, July 2016.

[40] K. Berntorp, "Path planning and integrated collision avoidance for autonomous vehicles," in *Proceedings of the 2017 American Control Conference (ACC)*, pp. 4023–4028, Seattle, WA, USA, May 2017.

[41] M. Ghazali, M. Durali, and H. Salarieh, "Vehicle trajectory challenge in predictive active steering rollover prevention," *International Journal of Automotive Technology*, vol. 18, no. 3, pp. 511–521, 2017.

[42] S. Li, Z. Li, B. Zhang, S. Zheng, X. Lu, and Z. Yu, "Path tracking for autonomous vehicles based on nonlinear model: predictive control method," in *Proceedings of the SAE Technical Paper 2019-01-1017*, Detroit, MI, USA, April 2019.

[43] T. Ming, W. Deng, S. Zhang, and B. Zhu, "MPC-based trajectory tracking control for intelligent vehicles," in *Proceedings of the SAE Technical Paper 2016-01-0452*, Detroit, MI, USA, April 2016.

[44] A. Y. Lee, "Performance of driver-vehicle in aborted lane change maneuvers," in *Proceedings of the SAE Technical Paper*, Warrendale, PA, USA, February 1996.

[45] P. Raksincharoensak, M. Nagai, and H. Mouri, "Investigation of automatic path tracking control using four-wheel steering vehicle," in *Proceedings of the IVEC2001. Proceedings of the IEEE International Vehicle Electronics Conference 2001. IVEC 2001 (Cat. No. 01EX522)*, pp. 73–77, Tottori, Japan, September 2001.